

Analytic Analysis of Irregular Discrete Universes

Shan W. Jolin

*Nanostructure Physics, Royal Institute of Technology
106 91 Stockholm, Sweden*

Kjell Rosquist

*Department of Physics, Stockholm University
106 91 Stockholm, Sweden*

Abstract

In this work we investigate the dynamics of cosmological models with spherical topology containing up to 600 Schwarzschild black holes arranged in an irregular manner. We solve the field equations by tessellating the 3-sphere into eight identical cells, each having a single edge which is shared by all cells. The shared edge is enforced to be locally rotationally symmetric (LRS), thereby allowing for solving the dynamics to high accuracy along this edge. Each cell will then carry an identical (up to parity) configuration which can however have an arbitrarily random distribution. The dynamics of such models is compared to that of previous works on regularly distributed black holes as well as with the standard isotropic dust models of the FLRW type. The irregular models are shown to have richer dynamics than that of the regular models. The randomization of the distribution of the black holes is done both without bias and also with a certain clustering bias. The geometry of the initial configuration of our models is shown to be qualitatively different from the regular case in the way it approaches the isotropic model.

1 Introduction

matter distribution in the universe is discrete and therefore strongly locally inhomogeneous, it is natural to ask how this affects the overall expansion rate. The question is to what extent the dynamics of the real universe is described by the homogeneous fluid FLRW models. Due to the nonlinear nature of the Einstein equations this is a difficult problem often referred to as the averaging problem in general relativity [1, 2]. It has been extensively discussed in the past but there is still no consensus about its solution (see e.g. [3]). A new avenue to address this issue was recently opened by considering a universe filled with Schwarzschild black holes as sources [4, 5, 8, 9, 12, 21]. The idea is to first specify the sources as initial data on a time-symmetric spatial hypersurface with spherical topology. It is possible to do this using a finite number of Schwarzschild black holes as an exact solution of the Einstein constraints. This configuration of initial data can then in principle be evolved using the Einstein evolution equations. While the general evolution can only be done numerically, some subsets with sufficiently high symmetry can be evolved exactly or approximately by analytical methods. The line of investigation is still in its infancy with no clearcut answer to the averaging issue. However, we believe that this approach has a promising potential in this respect. It may also illuminate other related issues, one being the role of interaction energies in many body systems.

In previous work on such cosmologies the focus has been on models with a regular matter configuration of the 4-polytope type. This kind of configuration has been used to simplify the analysis. The regular 4-polytopes are 4-dimensional analogues of the (3-dimensional) Platonic solids. There are six different regular 4-polytopes with 5, 8, 16, 24, 120 or 600 cells. Previous work on such regular

models placed identical sources at the cell centres. In this way the regularity of the model could be preserved. The edges of the cells in such a model have a high degree of symmetry in the sense that the gravitational field is locally rotationally symmetric (LRS) about the edge. The edge is then said to be an LRS curve [8]. This symmetry will allow an analytic analysis of the evolution up to some time away from the initial data hypersurface.

Our primary goal in this work is to relax the obviously unrealistic condition of regularity to see how this will affect the curvature structure and also the evolution. We wish to construct a model in which the sources can be distributed randomly while still preserving at least one LRS curve. It would not be possible to do this with a completely random distribution. However, the existence of LRS curves depends only on discrete symmetries. Each reflection symmetry has an associated symmetry surface (the mirror). If three or more such symmetry surfaces have a common intersection curve, then that curve is necessarily LRS [9]. Consider the regular 4-polytope with 16 cells as an example and fill one of its cells with a random distribution of sources. At an edge of that cell there are in total four cells that meet. One is the cell we have already filled and then there are three more cells meeting at that edge. We can now fill the other three cells by reflecting the given sources in the adjoining faces going around the edge. The newly filled cells can then be used as seeds to fill the rest of the polytope. Since there is an even number of cells at the edges, this procedure gives an unambiguous distribution of sources for the whole polytope. Each cell is then a mirror image of all its neighbours. However the distribution inside the cells can be arbitrarily irregular.

While the above construction works well it cannot be used for any other regular 4-polytope. The reason is that all the other polytopes have an odd number of cells meeting at the edges. In particular, it cannot be used for the 8-cell polytope which is the one that has been most extensively investigated in the past. For that reason we will use another model with eight identical cells which is also a tessellation of the 3-sphere but which is not of the regular polytope type. Instead, the cells can be characterized as solid lenses. All the cells meet at a great circle. If the number of cells is of the form $n = 6 + 2k$ with k a non-negative integer, then the common great circle retains the LRS property when the above construction of the source configuration is used. The choice $k = 1$ gives us an 8-cell model which contains the desired LRS curve.

We will use the second half of the Greek alphabet ($\mu, \nu, \rho \dots = 0, 1, 2, 3$) for spacetime coordinate indices and the second half of the Latin alphabet to indicate spatial coordinate indices ($i, j, k \dots = 1, 2, 3$). The first half of the Latin alphabet and the first half of the Greek alphabet will be used for spacetime orthonormal frame indices ($a, b, c \dots = 0, 1, 2, 3$) and spatial orthonormal frame indices ($\alpha, \beta, \gamma \dots = 1, 2, 3$) respectively.

1.1 The Initial Metric of the DI Model

Following [4] (see also [5]) we consider an initial *instantaneously static* spatial hypersurface with metric

$$h = \psi^4 \hat{h}_{ij} dx^i dx^j \quad (1)$$

where \hat{h} is the metric of a 3-sphere and ψ is a conformal factor to be specified below. In hyperspherical coordinates the metric has the form

$$\hat{h} = d\chi^2 + \sin^2 \chi (d\theta^2 + \sin^2 \theta d\phi^2) \quad (2)$$

with coordinates in the ranges $0 < \chi < \pi$, $0 < \theta < \pi$ and $0 \leq \phi < 2\pi$. For some purposes it is useful to embed the 3-sphere in a 4-dimensional Euclidean space with Cartesian coordinates (w, x, y, z) . The relations to the hyperspherical coordinates are

$$\begin{aligned} w &= \cos \chi \\ x &= \sin \chi \sin \theta \cos \phi \\ y &= \sin \chi \sin \theta \sin \phi \\ z &= \sin \chi \cos \theta . \end{aligned}$$

The point where $\chi = 0$ is referred to as the north pole of the hypersphere.

We will proceed as in [4] and solve the Gauss-Codazzi equations:

$$\begin{aligned} R + K^2 - K_{ij}K^{ij} &= 0 \\ (K_i{}^j - \delta_i{}^j K)_{|j} &= 0 \end{aligned} \quad (3)$$

where K_{ij} is the extrinsic curvature of the 3-space, K is its trace and R is the Ricci scalar of the (physical) 3-space. The vertical line in equation (3) denotes the (spatial) covariant derivative of the metric h . Since the hypersurface is instantaneously static, the extrinsic curvature vanishes, $K_{ij} = 0$, and the Gauss-Codazzi equations are then reduced to the very simple form

$$R = 0. \quad (4)$$

For the metric (1), this condition reduces to the Helmholtz equation on the 3-sphere

$$\hat{\nabla}^2 \psi = \frac{1}{8} \hat{R} \psi \quad (5)$$

where \hat{R} is the 3-sphere Ricci scalar and $\hat{\nabla}^2$ is the 3-sphere Laplacian. Since the Helmholtz equation is linear in ψ we can form a superposition of single black hole solutions. A conformal factor corresponding to N Schwarzschild masses on the background 3-sphere can be defined as

$$\psi(\chi, \theta, \phi) = \sum_{k=1}^N \frac{\sqrt{m_k}}{\sqrt{2(1 - n \cdot n_k)}} \quad (6)$$

where n and n_k are unit vectors in the embedding space. The location of each source is provided by the vector n_k while

$$n = (\cos \chi, \sin \chi \sin \theta \cos \phi, \sin \chi \sin \theta \sin \phi, \sin \chi \cos \theta). \quad (7)$$

The full hypersurface metric is then obtained by inserting the conformal factor (6) in (1).

1.2 Locally Rotationally Symmetric Curves

Locally Rotationally Symmetric (LRS) spacetimes have been defined and investigated rather extensively by several authors following [10]. A spacetime is LRS if the tangent space of every point has a direction about which there is no preferred perpendicular direction defined by the geometry. Here we consider spacetimes which are not LRS everywhere but contain curves of LRS points. Our DI models are constructed with symmetry surfaces whose intersections are LRS curves. Such curves are useful since they allow a significant simplification of the dynamics. Specifically, the dynamics for points on the LRS curves reduces to a system of ODEs driven by a non-autonomous term which can be evaluated (in principle) by a recursion procedure [9]. In practice, it has only been possible to evaluate the recursion a few steps before it becomes unwieldy. Nevertheless, even the undriven ODE system gives results that match current numerical work to an accuracy of about one percent [12].

Suppose that there are n surfaces which intersect along a curve and that the geometry admits reflection symmetry about each of the surfaces. Now arrange an orthonormal frame ($\mathbf{e}_1, \mathbf{e}_2, \mathbf{e}_3$) with \mathbf{e}_1 parallel to the curve. There will then be a discrete set of rotations about the curve such that the frame vectors are transformed as

$$\begin{aligned} \tilde{\mathbf{e}}_1 &= \mathbf{e}_1 \\ \tilde{\mathbf{e}}_2 &= \mathbf{e}_2 \cos \phi_q - \mathbf{e}_3 \sin \phi_q \\ \tilde{\mathbf{e}}_3 &= \mathbf{e}_3 \cos \phi_q + \mathbf{e}_2 \sin \phi_q \end{aligned} \quad (8)$$

while leaving invariant all tensors picked out by the geometry

$$T^{\tilde{a}\tilde{b}\tilde{c}\dots}_{\tilde{d}\tilde{e}\tilde{f}\dots} = T^{abc\dots}_{def\dots} \quad (9)$$

The rotation angles are given by $\phi_q = 2\pi q/n$ where $n \geq 2$ is the number of intersecting surfaces and $q = 1, \dots, n-1$. For $n \geq 3$ it can be shown that curves associated with such a discrete symmetry group have the LRS property [8] while for $n = 2$ this does not follow (see discussion in [5] and [9]). Vectors and tensors satisfying (9) have the following properties when evaluated along LRS curves:

1. For a vector T^α evaluated in the orthonormal frame we have $T^2 = T^3 = 0$ while T^1 remains arbitrary. Therefore vectors respecting the discrete symmetry group are always parallel to the LRS curve.
2. A rank-2 tensor with orthonormal components $T^{\alpha\beta}$ must be diagonal along an LRS curve with components satisfying $T^{22} = T^{33}$.

1.3 A Piecewise Statistically Uniform Distribution of Sources in a 3-Sphere Universe

We wish to construct a universe in which the sources are distributed as randomly as possible but still contains at least one LRS curve. We can then use the existence of the LRS curve to get estimates of the dynamics of the model. To satisfy the LRS requirement we need a model which has a symmetry subgroup containing at least three distinct reflection isometries. The symmetry surfaces in such a model leads to a lattice of cells which are identical up to reflections. Every cell face is then part of a symmetry surface for a reflection. For simplicity, consider a lattice with identical cells. One could then try to define a piecewise random source configuration as follows. First distribute N sources randomly in one of the cells. Then for each face of that cell reflect the given source distribution to a neighbouring cell using the reflection symmetry corresponding to that face. Further reflections can then be used to distribute the given source configuration to all the cells in the model. For such a construction to work, the relevant symmetry subgroup of the model must be preserved when all the cells have been filled. Otherwise, the LRS property will not in general be preserved. It is straightforward to see that a necessary condition for this is that the number of cells meeting at an edge must be even. The number in question is the third Schläfli number. Of the regular models in [4], only the 16-cell satisfies the requirement with four cells meeting at the edges. It can be shown explicitly that the above construction does work for the 16-cell. However, we prefer to use a different model that contains only eight cells and for which there is a simple algorithm that can be used repeatedly to populate the cells.

1.3.1 Tessellating the 3-Sphere

Similarly to [4], we consider a 3-sphere representing a momentarily static hypersurface in the universe. It is tessellated into a set of empty and identical cells. However, unlike in [4], the tessellation in our case will not correspond to any of the regular polytopes but will instead be taken to resemble hyperspherical versions of “orange pieces”.

Suppose we have an orange and intend to share it by cutting it into a number of wedge pieces. Typically one might make the cuts where the black curves are in figure 1 which would result in several manageable pieces. If one ensures that each piece is of the same size, the number of pieces will be determined by the “equatorial width” $\Delta\phi$.

In terms of a general 2-sphere instead of an orange, the surface of each orange piece corresponds to a cell, while the knife cuts are cell boundaries. The cell boundaries are located at fixed ϕ -coordinates and the angular distance to the nearest cell boundary is given by $\Delta\phi$, which must be equal for all cells. In addition, all cell boundaries intersect at two points - the north and south pole.

Keeping this image in mind, we now make our move to the 3-sphere. In this transition surfaces become volumes, curves become surfaces and points become curves. Thus our “orange” becomes a 3-sphere, with 3-dimensional cells, each bounded by two 2-dimensional spherical surface segments. These cell boundaries intersect along a curve C_{LRS} (instead of at merely two points) which is a great circle passing through the 3-sphere’s north and south poles located at $\chi = 0$ and $\chi = \pi$ respectively.

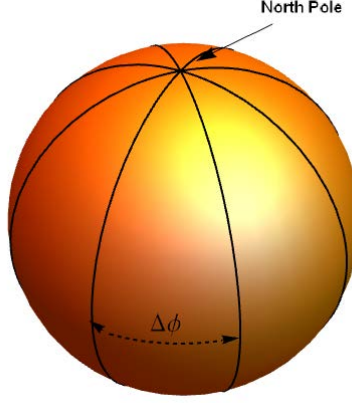


Figure 1: If a 2-sphere represents an orange peel, the black curves then represent knife cuts. The surface of each resulting peel segment is then considered a cell and the cuts are cell boundaries. The dashed line indicates the “equatorial width” $\Delta\phi$ which is taken to be the same for all cells. The poles are located opposite each other at the intersection of the cell boundaries.

In Cartesian coordinates (w, x, y, z) the curve C_{LRS} is parametrized by

$$C_{LRS} = (\cos \lambda, 0, 0, \sin \lambda) \quad \text{where} \quad 0 \leq \lambda < 2\pi. \quad (10)$$

The cell boundaries ∂V_q are a series of spherical surface segments which enclose the 3-dimensional cells V_q . Using hyperspherical coordinates (χ, θ, ϕ) , the cell boundaries ∂V_q are given by

$$\partial V_q = (\chi, \theta, \frac{\pi}{p}q) \quad \text{where} \quad p \geq 3 \quad \text{and} \quad q = 0, 1, \dots, 2p-1. \quad (11)$$

The integer p corresponds to the number of intersecting surfaces (cell boundaries). The form of each cell can be viewed as similar to a biconvex spherical lens (cf. [20]).

1.3.2 Filling the cells

After tessellating the 3-sphere as described above, the resulting cells are to be filled with a number of Schwarzschild black holes in a manner which ensures that the curve C_{LRS} actually remains LRS. We do this by first designating one of the cells as a *starting cell* (this choice is completely arbitrary since all cells are identical). Then fill the starting cell with one or more points (corresponding to the location of sources, specifically black holes) in any desirable manner. We choose to distribute the points randomly in the starting cell by using an algorithm invented by Marsaglia [6]. The algorithm is designed to generate random uniform distributions on the 3-sphere.

1. First select four points V_1, V_2, V_3 and V_4 randomly from the interval $[-1, 1]$ and ensure that $S_1 = V_1^2 + V_2^2 < 1$ as well as $S_2 = V_3^2 + V_4^2 < 1$.
2. Then the following point is picked randomly from a uniform distribution on the unit 3-sphere:

$$w = V_4 \sqrt{\frac{1 - S_1}{S_2}}, \quad x = V_1, \quad y = V_2, \quad z = V_3 \sqrt{\frac{1 - S_1}{S_2}}. \quad (12)$$

3. If it lies outside the starting cell - discard it. Otherwise - keep the point. Initially we only want points inside our starting cell.
4. Repeat steps 1-3 until a desirable number of points lie inside the starting cell.

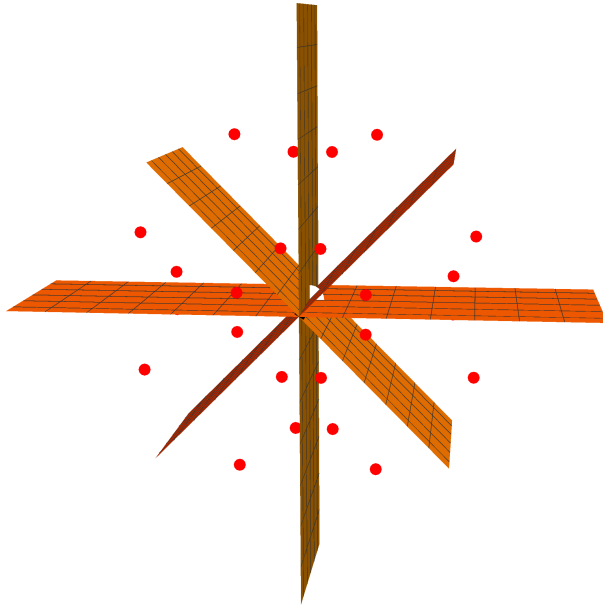


Figure 2: Stereographic projection of our 3-sphere tessellated into 8 cells. The planes are the cell boundaries and the points correspond to black holes while the white point in the middle indicates the location of the south pole at $\chi = \pi$. Notice that the contents of each cell is a mirror image of its neighbour, since the cell boundaries permit reflection symmetry by construction. The planes intersect each other along a line which corresponds to the LRS curve. Notice also the discrete rotational symmetries that exist for rotations about the intersection line. To be specific, there are 4 distinct rotations (multiples of $\pi/2$, *cf.* (11)) about that line leaving the space invariant.

After the starting cell has been filled with a random configuration of points, the remaining cells are filled with a point configuration such that every cell becomes the mirror image of its neighbour. This is most easily done in the stereographic projection of the 3-sphere, where the cell boundaries are flat surfaces instead of spherical - see figure 2. Since the cell boundaries are symmetry surfaces, the configuration of the starting cell can easily be mirrored into the neighbouring cells. Once every cell is a mirror image of its neighbour, an inverse of the stereographic projection can be made to return to the original 3-sphere. The cells will still remain mirror images of each other since the projection is conformal. Furthermore since two reflections correspond to a rotation there will also be a discrete rotational symmetry around the common cell boundary C_{LRS} [7].

1.3.3 The Specifications of our Model

We have chosen to investigate the dynamics of a DI orange piece model consisting of 8 cells corresponding to $p = 4$. This is a model with few cells which is also comparatively simple to handle technically when defining the source distributions. In addition, having 8 cells allow us to compare with regular models in [8] in which the total number of masses investigated were 8, 16, 24, 120 or 600 (corresponding to 1, 2, 3, 15 or 75 masses per cell respectively).

2 Finding the Proper Mass of Schwarzschild Black Holes in the DI Model

In paper [4], two types of mass were discussed, *viz.* the effective mass and the proper mass. The effective mass m_{eff} corresponds to the mass parameters m_k in (6). It is the mass the source would have if it were alone in an asymptotically flat universe. However when multiple masses are present, m_{eff} will also contain interaction energies (which are negative). In this paper, the effective mass is set to a constant. The reasoning behind this is simplicity - it is easier to calculate proper mass from a fixed

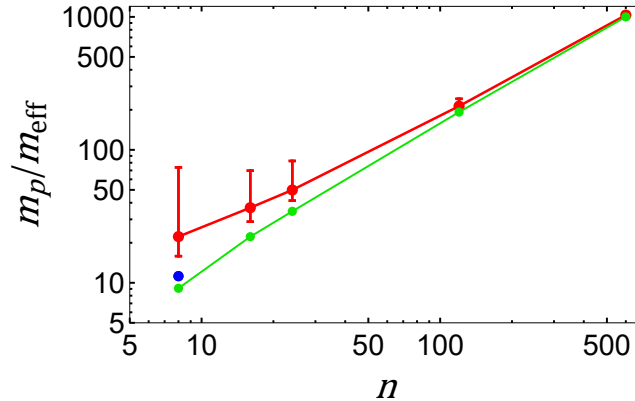


Figure 3: Mass ratios m_p/m_{eff} plotted against the number of masses n obtained from more than 200 randomly generated configurations. The red curve shows the median mass ratios and the error bars indicate the quintiles. For 8 sources, there is the possibility to have one source at the center of each cell. This is the closest our DI model can approximate the regular 8-source model in [4] and is indicated by the blue dot. The green curve depicts the regular ratios found in the aforementioned paper.

effective mass rather than the other way around. The actual value of m_{eff} will then simply correspond to an overall scaling of all the masses. We therefore present the data as the ratio m_p/m_{eff} .

The proper mass is defined as in [4] and is analogous to the concept of bare mass in [14]. Physically it can be interpreted as the “local” mass as measured in a vicinity of the black hole. The difference between the two mass concepts can be interpreted as due to the interaction energies between all the sources in the configuration. The proper mass of a Schwarzschild black hole at $\chi = 0$ (north pole) is calculated by expanding the conformal factor (6) according to

$$\sum_{k=1}^N \frac{\sqrt{m_k}}{\sqrt{2(1 - n \cdot n_k)}} = \frac{2c_1}{\chi} + c_2 + O(\chi) \quad (13)$$

where c_1 and c_2 are constants depending on the mass configuration. The proper mass is then given by [19]

$$m_p = 4c_1c_2. \quad (14)$$

The proper mass of sources at other positions can be calculated by first rotating the coordinate system (or the mass configuration) to place the north pole at a given source.

Referring to the expansion (13) it is clear that the proper mass depends on the configuration of sources – different configurations will yield different proper mass values. Since any source configuration is randomly generated, a wide range of proper masses can be expected. We proceed by randomly generating many (over 200) configurations and calculating the proper mass of the sources.

However, not all sources in a given configuration need to be accounted for. Any source in one cell and its counterpart in every other cell are equally “massive”, because each cell are identical up to a rotation or reflection. It is therefore not necessary to study *all* proper masses in a given configuration, only those inside a single cell.

We have chosen to characterize the distributions by their median, and upper and lower quintiles (which separates the highest, respectively the lowest, 20% of the data from the remaining 80%). These are then plotted as a function of the number of sources n , as done in figure 3. We can also compare with the mass ratios obtained for the regular models in [4]. Clearly the mass ratios for the DI and the regular model converge for large n [4, 8] and become more massive. It therefore appears that the overall interaction energies of the DI model are approaching those of the regular configuration in the limit of large n .

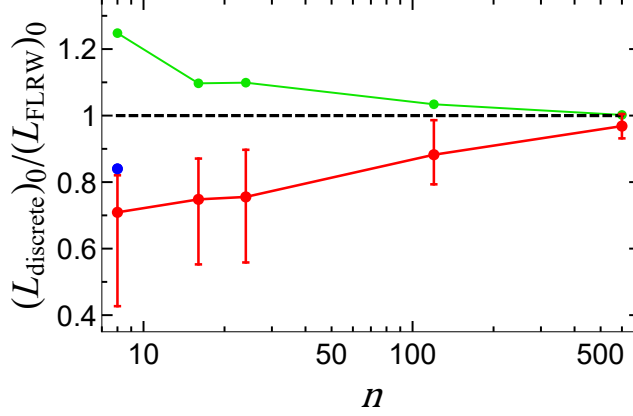


Figure 4: Comparison of the (LRS) curve lengths in the DI model and the FLRW model as a function of source count n . The red curve depicts the lengths in the DI model $(L_{\text{DI}})_0$ and error bars indicate the quintiles. The green curve depicts the length in the regular models $(L_{\text{regular}})_0$ in [4]. The dashed horizontal line corresponds to the FLRW model. The blue dot corresponds to the DI model with a single source at the center of each cell. On the vertical axis - the symbol $(L_{\text{discrete}})_0$ is a placeholder for either $(L_{\text{regular}})_0$ or $(L_{\text{DI}})_0$. The zero subscript indicates that the lengths are calculated on the initially time-symmetric hypersurface at $t = 0$.

3 Initial Behaviour on the LRS Curve

3.1 Initial Length of the LRS Curve

The initial length of the LRS curve is simple to calculate, since the curve is a great circle which can be parametrized by χ in hyperspherical coordinates. Using the metric given by the expressions (1) and (6), the LRS curve length is then given by the integral

$$L_0^{\text{DI}} = 2 \int_0^\pi \psi^2(\chi, 0, \phi) d\chi. \quad (15)$$

A factor of two arises since both halves of the LRS curve are identical (due to reflection symmetry) and the above integral only takes half of the curve into account.

This can be compared to the spherical matter-dominated FLRW model (with no dark energy present) at the moment of maximum expansion:

$$dl^2 = \frac{16M^2}{9\pi^2} (d\chi^2 + \sin^2 \theta d\theta^2 + \sin^2 \chi \sin^2 \theta d\phi^2). \quad (16)$$

In this geometry, the length of a great circle with the same parametrizations as mentioned above is

$$L_0^{\text{FLRW}} = 8M/3, \quad (17)$$

where M is the total (proper) mass in the universe.

Figure 4 plots the ratio between the LRS curve length in the DI model and the FLRW model as a function of the number of sources. The length in the FLRW model is computed according to equation (17) where M is the total proper mass in the DI model (obtained using the method in section 2). The large dots indicate the median, while the accompanying error bars indicate quintiles. For histograms detailing the length distributions in detail, see [7]. By including data for the regular models from [4], we see that both model types approach the FLRW limit as more sources are added. Our results are so far consistent with [23], where a thorough analysis is made of the continuum limit. However, while the regular models approach the FLRW limit from above, the irregular models approach it from below.

There are thus two different ways to approach the limiting homogenous case presented by the FLRW model.

A possible cause for these two types of behaviours can be found by examining figure 8 in [24]. In that work, a cosmological model with clusters of black holes and a tessellation identical to that in [4] is studied. There the authors also observe an approach to the FLRW limit from above. This observation suggests that the choice of tessellation of the 3-sphere will affect how the FLRW limit is approached.

3.2 Initial Curvature Along the LRS Curve

The DI models, being vacuum universes only support Weyl curvature. This is in contrast to FLRW models which have only Ricci curvature as a consequence of their conformally flat nature. The Weyl curvature tensor $C_{\mu\nu\rho\sigma}$ can be invariantly decomposed in two parts, a gravito-electric part $E_{\mu\nu}$ and a gravito-magnetic part $H_{\mu\nu}$. They are defined by the relations

$$E_{\mu\nu} := C_{\mu\rho\nu\sigma}u^\rho u^\sigma, \quad H_{\mu\nu} := {}^*C_{\mu\rho\nu\sigma}u^\rho u^\sigma \quad (18)$$

where u^μ is a 4-velocity field representing an observer family and ${}^*C_{\mu\rho\nu\sigma}u^\rho u^\sigma$ is the dual Weyl tensor. The latter is given by

$${}^*C_{\mu\nu\rho\sigma} := \frac{1}{2}\eta_{\mu\nu}{}^{\kappa\tau}C_{\kappa\tau\rho\sigma} \quad (19)$$

where $\eta_{\mu\nu\rho\sigma}$ is the Levi-Civita tensor. The tensors $E_{\mu\nu}$ and $H_{\mu\nu}$ are symmetric and traceless by their definition. Their definition also implies the relations $E_{\mu\nu}u^\nu = 0$ and $H_{\mu\nu}u^\nu = 0$. This shows that they are spatial tensors lying in the rest spaces of the u^μ observers. At the initial momentarily static hypersurface, the gravito-magnetic field is zero while the gravito-electric field equals the traceless part of the intrinsic Ricci 3-curvature of the initial hypersurface, $E_{\mu\nu} = {}^{(3)}R_{\mu\nu}$ (see e.g. [8]).

We follow the convention [11] and define the following five variables representing the orthonormal components of any symmetric tracefree spatial rank-2 tensor (using the gravito-electric tensor $E_{\alpha\beta}$ as an example): $E_+ = -\frac{3}{2}E_{11}$, $E_- = \frac{\sqrt{3}}{2}(E_{22} - E_{33})$, $E_1 = \sqrt{3}E_{23}$, $E_2 = \sqrt{3}E_{31}$ and $E_3 = \sqrt{3}E_{12}$. However, taking \mathbf{e}_1 to be directed along the LRS curve, tracefree symmetric rank-2 tensors are diagonal with $E_- = 0$. Therefore the quantity E_+ is the only nonzero curvature component along the LRS curve. We will investigate the behaviour of $(E_+)_0$ along the LRS curve on the initial static hypersurface with the zero subscript indicating evaluation at $t = 0$.

The LRS curve, as we have defined it, is located at $\theta = 0, \pi$. However, as is evident from Eq. 1, the determinant of the metric is zero where $\theta = 0, \pi$ implying that the entire curve is located at a coordinate singularity. Therefore, to calculate the curvature, we first rotate the configuration such that the LRS curve instead lies at $\chi = \theta = \pi/2$ and is parametrized by $\phi \in [0, 2\pi]$. Therefore in the ensuing graphs, the position on the LRS curve is given by the hyperspherical coordinate ϕ .

Figures 5 - 6 show some examples of how the quantity $(E_+)_0$ behaves along the LRS curve. It can be seen that in some cases the sign of $(E_+)_0$ changes. To compare with the regular models of Ref. [8] we can consider the sign of $(E_+)_0$ along the edges of the cells in that paper, noting that it is negative. Further remarks about the sign distribution can be found at the end of this section. We will also return to discuss a physical interpretation of the sign of $(E_+)_0$ when treating time evolution in Sect. 4

Now let us take a look at each case individually. From figure 5 we see a unique behaviour exhibited when only 8 sources are present, namely the curvature is constant! This is always the case for any configuration consisting of only 8 sources: the curvature is constant with $(E_+)_0 < 0$. The reason behind the constant curvature is most likely due to the topology of the 3-sphere.

For 16 and 24 masses, the behaviour of $(E_+)_0$ becomes more mixed - maxima and minima with occasional changes in the sign of $(E_+)_0$ are present. Furthermore the behaviour varies with different configurations. However, something which is consistent among different configurations is the number of local maxima and minima. For 16 sources the number of maxima found on the LRS curve is two, which is the number of masses per cell. Similarly for 24 sources the number of maxima is three - also the number of masses per cell. This is evident in figure 5. Due to the relatively small number of sources, the effect of each black hole is distinctly visible.

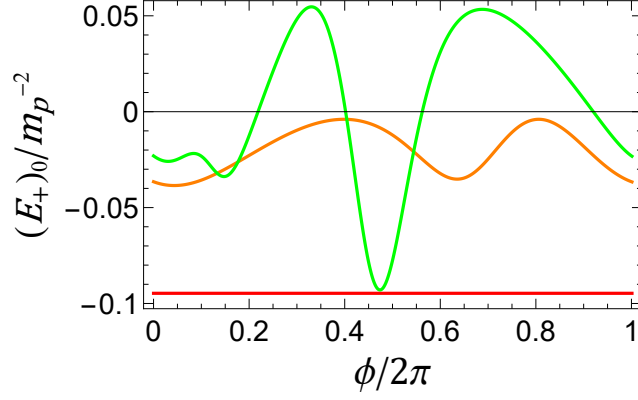


Figure 5: The curvature $(E_+)_0$ along the LRS curve for three example configurations. Each curve corresponds to a single configuration with 8 (red), 16 (orange) and 24 (green) sources respectively. The curvature is scaled by the inverse square of the median proper mass m_p of the corresponding configuration.

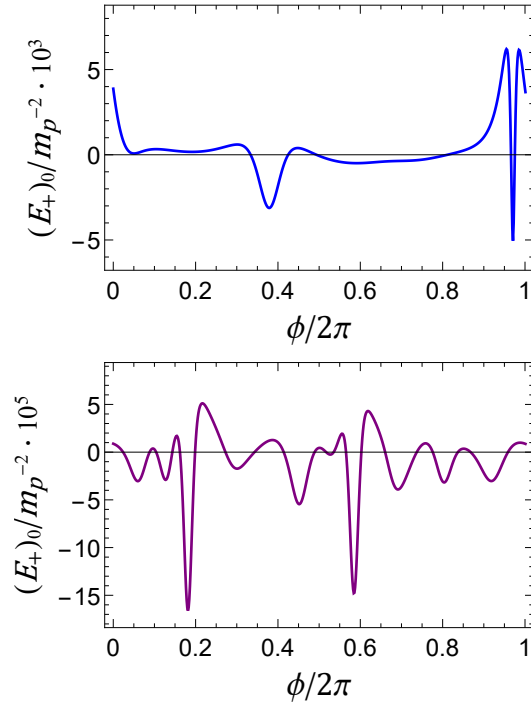


Figure 6: The curvature $(E_+)_0$ along the LRS curve for an example case with 120 sources (top) and 600 sources (bottom). The values are scaled by the median proper mass m_p .

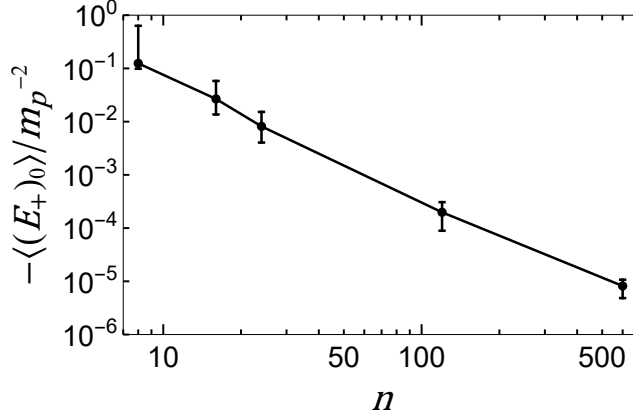


Figure 7: The curvature averaged along the LRS curve $\langle (E_+)_0 \rangle$ in units of inverse median proper mass squared. This average is not unique for a given number of sources n , but depends on the configuration. The plot above presents the result after generating many random configurations, which yields a distribution. As usual in this paper, dots and error bars indicate *median* and quintiles of this distribution, respectively.

For 120 and 600 masses, the $(E_+)_0$ behaviour is even more dramatic and irregular. Figure 6 displays positive peaks and negative troughs and Riemann flat points at $(E_+)_0 = 0$. The latter points are characterized by a vanishing Riemann tensor. The spike-like features are most likely due to a nearby black hole horizon, cf. figure 13 in [8].

Finally we investigate the sign dominance of $(E_+)_0$ on the LRS curve. The sign of $(E_+)_0$ at a given point affects the time evolution of any point along the curve. Since there are different signs along the same curve, it follows that different regions might evolve differently [8]. A very rough estimate of the sign dominance is provided by the sign of the mean $\langle (E_+)_0 \rangle$. Figure 7 presents the median and the location of quintiles obtained from $\langle (E_+)_0 \rangle$, as a function of the number of masses. Negative values are clearly the most prevalent, approaching $\langle (E_+)_0 \rangle = 0$ when there are many sources in the model.

4 Time Evolution

4.1 Equations Governing Dynamics

With the initial conditions studied, we now proceed to evolve them. We restrict attention to the LRS curve for which the evolution can be studied by analytical methods. The evolution is governed by the system of ordinary differential equations [8, 9]

$$\frac{\ddot{a}_{\parallel}}{a_{\parallel}} = \frac{2}{3}E_+ \quad (20)$$

$$\frac{\ddot{a}_{\perp}}{a_{\perp}} = -\frac{1}{3}E_+ \quad (21)$$

$$\dot{E}_+ + 3\frac{\dot{a}_{\perp}}{a_{\perp}}E_+ = C_+(t) \quad (22)$$

where

$$C_+(t) = -\frac{3}{2}n^a n^b \text{curl} H_{ab} . \quad (23)$$

Here n^a is a unit vector along the LRS curve and

$$\text{curl} H_{ab} = \epsilon_{cd(a} D^c H^d{}_{b)} \quad (24)$$

and D_a is the spatial covariant derivative. The quantities a_{\parallel} and a_{\perp} are the scale factors parallel and perpendicular to the LRS curve. Although the $\text{curl} H$ term depends on spatial derivatives it can

be computed recursively term by term as a Taylor series in t (for given initial time-symmetric data) using the full Einstein vacuum equations (see [9] for details). Therefore, the system (20)–(22) can be considered as an autonomous ODE system driven by the explicitly time-dependent $\text{curl}H$ term. The initial values of the scale factors on the time-symmetric hypersurface (at $t = 0$) can be taken to be $(a_{\parallel})_0 = (a_{\perp})_0 = 1$ and the time-symmetry implies $\dot{a}_{\parallel} = \dot{a}_{\perp} = 0$. The initial values of the gravitoelectric field is given for each spatial position by $(E_+)_{\text{0}} = -\frac{3}{2}[(^{(3)}R_{11})]_{\text{0}}$.

Considering first the vertex points in the regular models (see [8]) we note that they are points of local spherical symmetry. Then any tensor object picked out by the geometry can only have a scalar part at the vertex. This implies in particular that $E_{ab} = H_{ab} = 0$. Therefore, the vertex points can be characterized as being Riemann flat. It then follows from Eqs. (20)–(21) that the scale factors are constant for all time, $a_{\parallel}(t) = a_{\perp}(t) = 1$.

Next we note that $\text{curl}H_{ab}$ is an odd function of t and that the Taylor expansion of (23) takes the form

$$C_+(t) = \sum_{n=1}^{\infty} \frac{C_+^{(2n+1)}}{(2n+1)!} t^{2n+1} \quad (25)$$

where the first nonzero term is of order t^3 [9]. In [8], Clifton *et al.* analyzed the autonomous part of the system (20)–(22) (i.e. with $C_+(t)$ assumed to vanish identically) for all the regular lattice configurations. By performing a numerical integration of the full Einstein system, Korzyński *et al.* [12] showed that the error incurred by neglecting the $\text{curl}H$ term in (22) is about 1% at $t \sim 3m_p$ when evolving a_{\parallel} and a_{\perp} at an edge midpoint in an 8-cell lattice. An analytic expression for the first term in (25) was given in [12] as a function of the conformal factor with respect to flat space. Covariant expressions for the first two terms were given in [9], the first one being

$$C_+^{(3)} = -6 n^a n^b \text{curl curl}(E^2)_{ab}|_{t=0} \quad (26)$$

where $(E^2)_{ab} = E_{ac}E^c_b$. To analyse our model, we will exploit the analytical solution of the undriven part of the system (20)–(22) given in [8]. In Sect. 6, we will estimate the error incurred by neglectation of the driving term. From the physical point of view, this approximation amounts to neglecting the gravitomagnetic effects, i.e. the part of the gravitational interaction which emanates from the relative motion of the masses.

Turning now to the case of nonzero curvature, we note that the undriven form of (22) is solved by $E_+ = (E_+)_{\text{0}}/a_{\perp}^3$. When $(E_+)_{\text{0}} > 0$, the scale factors can be expressed in terms of conformal time η by

$$\begin{aligned} a_{\perp} &= \cos^2 \eta \\ a_{\parallel} &= \frac{1}{2}(3 - \cos^2 \eta + 3\eta \tan \eta) \\ t - t_0 &= \frac{1}{\sqrt{\frac{2}{3}(E_+)_{\text{0}}}}(\eta + \frac{1}{2} \sin 2\eta) \end{aligned} \quad (27)$$

where $-\frac{\pi}{2} < \eta < \frac{\pi}{2}$ and t_0 is the constant of integration. In the case $(E_+)_{\text{0}} < 0$, the solution is given by

$$\begin{aligned} a_{\perp} &= \cosh^2 \eta \\ a_{\parallel} &= \frac{1}{2}(3 - \cosh^2 \eta - 3\eta \tanh \eta) \\ t - t_0 &= \frac{1}{\sqrt{-\frac{2}{3}(E_+)_{\text{0}}}}(\eta + \frac{1}{2} \sinh 2\eta) . \end{aligned} \quad (28)$$

where $-\frac{\pi}{2} < \eta < \frac{\pi}{2}$.

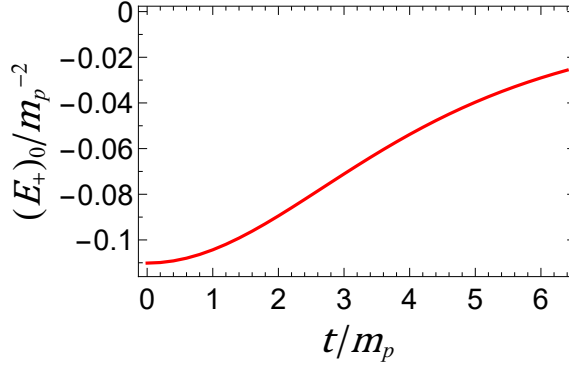


Figure 8: The time-evolution of E_+ for 8 masses at a fixed point on the LRS curve. The initial value $(E_+)_0$ is given in figure 5. Since the curvature is constant in this case, it is sufficient to study the behaviour at a single point on the LRS curve (see text). Both axes are scaled by the median proper mass m_p of the configuration.

4.2 Evolving E_+ on the LRS Curve

The equations given in section 4.1 allow us to study the curvature, measured by E_+ , as a function of time. A first example is given in figure 8, where we evolve a model with 8 sources. In that case, since the curvature is constant along the LRS curve (see figure 5), it is sufficient to evolve a single point on the curve. The value of E_+ increases monotonically until a coordinate singularity appears along the entire LRS curve simultaneously, beyond which our current formalism provides no information.

We have evolved the models with 16 and 24 sources for which initial data was plotted in figure 5. The result is displayed in figure 9. The time and the curvature E_+ in those figures are scaled by appropriate powers of the median proper mass m_p . All points on the LRS curve will eventually encounter a singularity unless initially Riemann flat (i.e. $(E_+)_0 = 0$). The sign of the curvature does not change along the part of the evolution that we can follow.

Referring to the evolution of models with 8, 16 and 24 sources (see figure 9) it appears that coordinate singularities appears before curvature singularities. This turns out to be the most common behaviour for the models that we have investigated. See figure 10 in which the first appearance of either a coordinate or curvature singularity is illustrated.

4.3 Dynamic Contractions and Expansions of the LRS Curve

We now proceed to study the length of the LRS curve (i.e. the LRS circumference) as a function of time. It is calculated by

$$\begin{aligned}
 L(t) &= \int_0^\pi a_{\parallel}(t) \psi^2(\chi, 0, \phi) d\chi + \int_0^\pi a_{\parallel}(t) \psi^2(\chi, \pi, \phi) d\chi \quad (\theta = 0, \pi) \\
 L(t) &= \int_0^{2\pi} a_{\parallel}(t) \psi^2(\pi/2, \pi/2, \phi) d\phi \quad (\chi = \theta = \pi/2)
 \end{aligned} \tag{29}$$

which is essentially equation (15) multiplied by a scale factor. Note that $a_{\parallel}(t)$ has an implicit position dependence as described in section 4.1. In particular, depending on the sign of $(E_+)_0$, the scale factors will have qualitatively different time evolution.

The LRS circumference is plotted as a function of time in figure 11 for 500 randomly generated models containing 8 sources. The lengths are scaled by the circumference $(L_{FLRW})_0$ of a great circle in a spherical FLRW model with the same total proper mass M_p . They are evolved until a singularity appears. The similarity in the form of the curves reflects the scaling of time caused by different initial

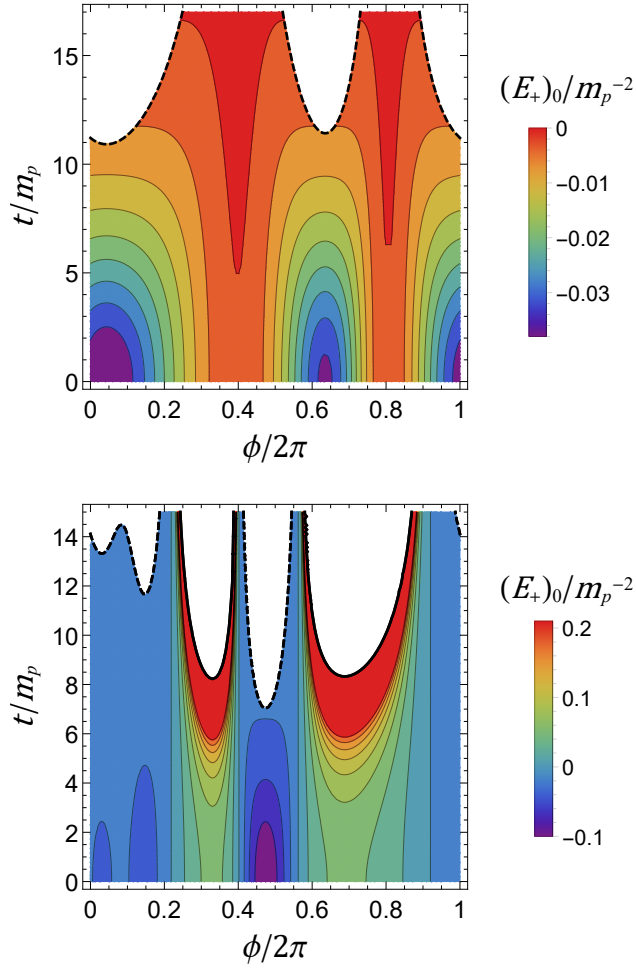


Figure 9: Density plot of the curvature for a configuration of 16 sources (top) and 24 sources (bottom). Here, ϕ is the angular position on the LRS curve (a great circle). Dashed black curves indicate the location of coordinate singularities, while solid black curves indicate curvature singularities. See figure 5 for a plot of the initial curvature of this configuration.

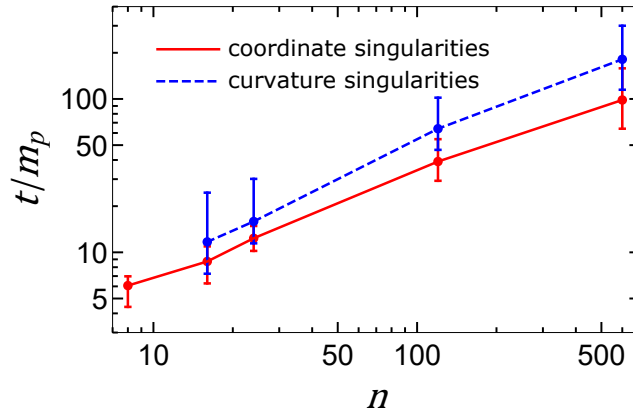


Figure 10: The median time it takes for a singularity to arise somewhere on the LRS curve as a function of the number of masses n . The error bars indicate as usual the quintiles.

8 sources

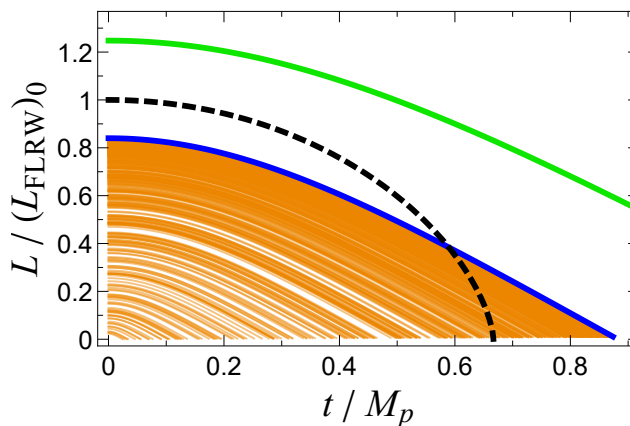


Figure 11: The circumference of 500 LRS curves as a function of time for 8 sources. Each orange curve corresponds to a randomly generated DI model. The blue curve illustrates the model with sources located at cell centers. The green and dashed black curve depict the regular model with 8 sources given in [8] and the spherical matter dominated FLRW model respectively.

values of E_+ in (28). The density distribution of the curves can be attributed to both the dependence on the position of the (single) source in the cells and to the nonlinear (square root) dependence on $(E_+)_0$ in (28).

A richer variety of dynamics can be seen for the remaining cases shown in figures 12. Looking at them, we can identify two general qualitative categories. The first category consists of curves which decrease monotonically with time, such as the FLRW case and models with regular configurations. A majority of the DI models exhibits this behaviour. The second category consists of curves which, at some point in time start to increase. This represents a turnaround in which the space in a neighbourhood of the LRS curve undergoes a change from contraction to expansion. This behaviour drastically deviates from the FLRW model and the regular cases. We cannot say if this is representative of the entire universe or if it is a semi-local anomaly.

4.4 Hubble and Deceleration Parameters

There are two additional parameters we can measure which enables further comparisons with FLRW cosmology. These are the Hubble and deceleration parameters which we define as

$$\mathcal{H}_L := \frac{\dot{L}}{L} \quad (30)$$

$$q_L := -\frac{\ddot{L}L}{\dot{L}^2} \quad (31)$$

where L is the length of the LRS curve. These two parameters are plotted for all the models we consider in figures 13-14. The black dashed curve depicts as usual the spherical FLRW case. In the 8 source model (figure 13), all curves show the same qualitative behaviour due to the position independent curvature. Even though this case is very different from the FLRW model in terms of size (see figure 4), it is qualitatively very similar.

In the remaining models (figure 14) the dynamics are more complex. Turning our attention to the deceleration parameter, we can broadly divide the behaviour in two categories. First we have all the curves for which the deceleration parameter is always positive. An example is provided in figure 15a. The curve starts at positive infinity before approaching zero. The FLRW curve and the regular models belong to this category, as well as a majority of the DI models.

The second category is characterized by the presence (at some point in time) of negative deceleration parameters. These curves are usually positive initially. An example is shown in figure 15b. In rare

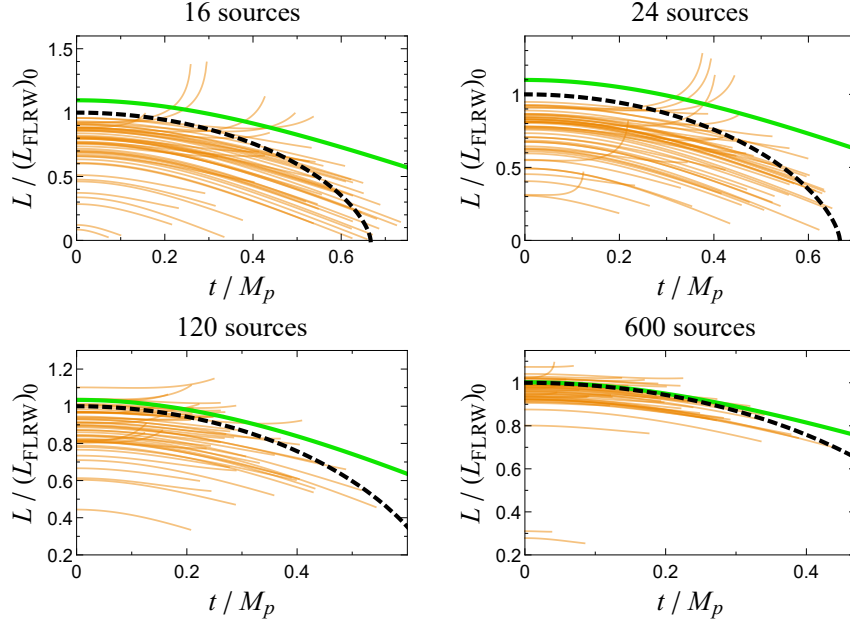


Figure 12: Circumference of LRS curves for configurations consisting of 16 masses (orange). The green and black curve depicts the regular model with 16 sources found in [4] and the spherical matter dominated FLRW model respectively.

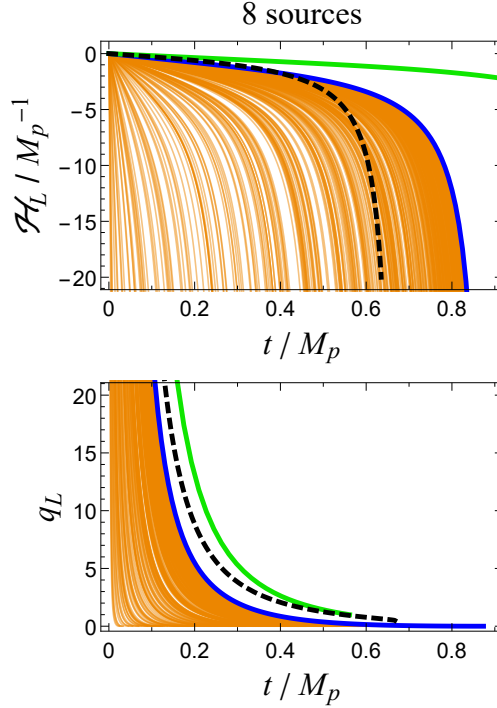


Figure 13: Figure depicting the Hubble parameter and the deceleration parameter for 500 randomly generated configurations consisting of 8 sources each. In the blue case, the source is located at the cell center. The green and dashed curves respectively refer to the regular model with 8 sources given in [4] and the spherical matter dominated FLRW model.

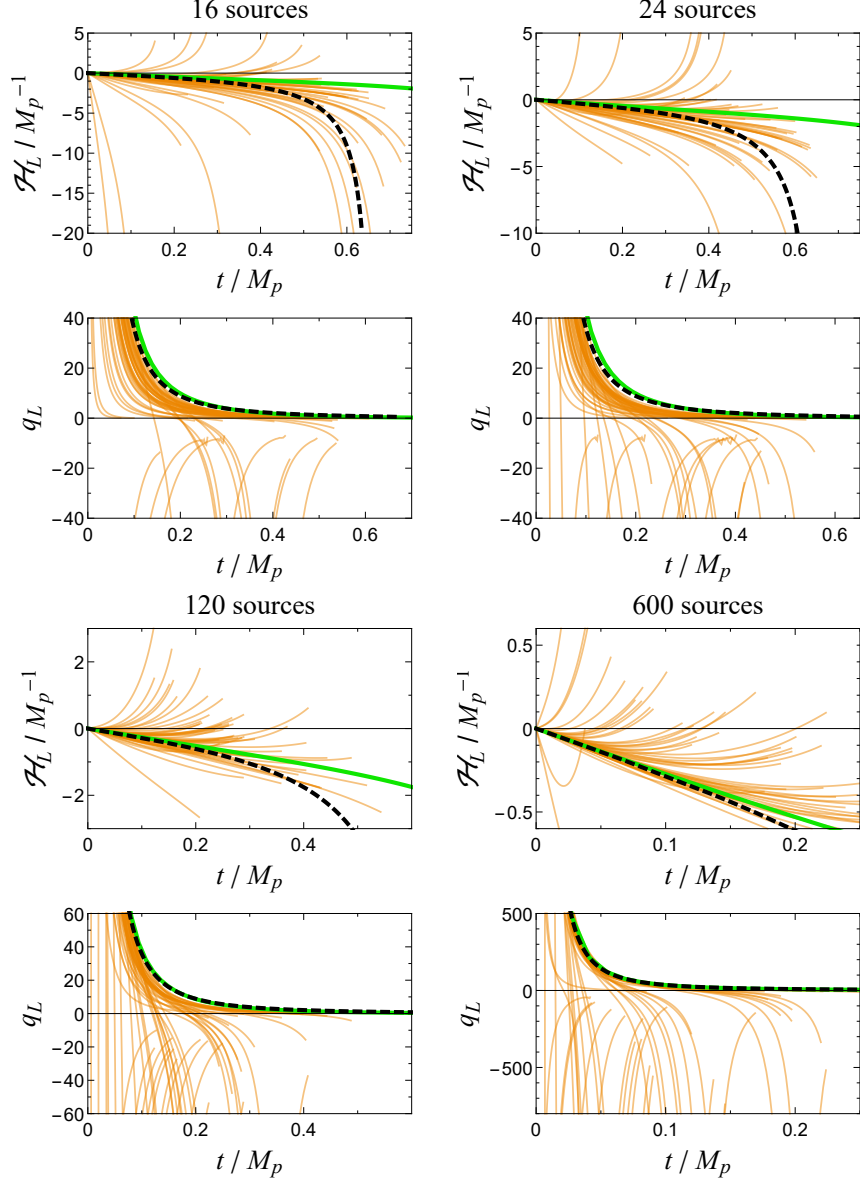


Figure 14: Figures depicting the Hubble parameter and the deceleration parameter for 50 randomly generated configurations consisting of 16 - 600 sources (orange). The green and black curves depict the regular models with corresponding number of sources, found in [4], and the spherical matter dominated FLRW model respectively.

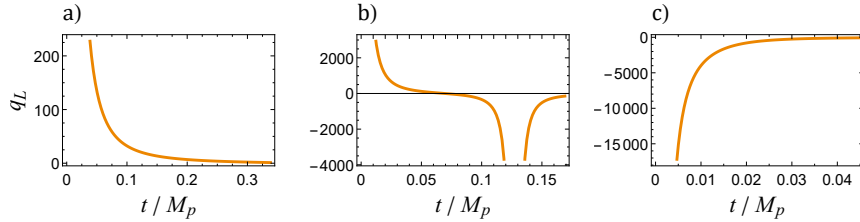


Figure 15: Three possible behaviours of the deceleration parameter with 600 sources. Panel a) shows only positive values while b) switches sign at some later time. The singularity in b) is due to a vanishing first derivative (see equation (31)). These are the most common types. We encounter occasionally deceleration parameters which are always negative, as depicted in c).

cases can we find models with always negative deceleration parameters, as in figure 15c. Regardless, the appearance of negative deceleration parameters is interesting, since in FLRW cosmology, negative values correspond to the presence of some exotic matter such as dark energy [13]. We show however that acceleration can occur across large regions of space in models with only ordinary mass (specifically Schwarzschild black holes) for some matter configurations.

Another interesting observation can be discerned from figures 13-14. From the Hubble parameters we see that the fraction of orange curves which terminates below the FLRW curve (black dashed curve) decreases as the source count increases. This provides a crude indication that the mean behaviour of the Hubble parameter becomes less Friedmann-like at late times as we increase the source count (if the mean was Friedmann-like, we would expect an equal number of curves to terminate above and below the FLRW case).

A valid question is whether or not our results would change if we would have included the $\text{curl}H$ term. However, we know that the error starts from zero (being of order $\sim t^3$ initially), and as demonstrated in [12] and to be illustrated in section 6, the gravitomagnetic effect is very small.

5 Fitting the Friedmann Equation

The Friedmann equation for a late time flat cosmology consisting of dark energy and ordinary matter can be expressed as [13]

$$\left(\frac{\dot{a}}{a}\right)^2 = H_0^2 \left(\Omega_{M_0} \left(\frac{a_0}{a}\right)^3 + \Omega_{\Lambda_0} \right) \quad (32)$$

where Ω_{M_0} and Ω_{Λ_0} are the density parameters corresponding to mass and dark energy respectively. Furthermore the relationship between the density parameters are

$$\Omega_{M_0} + \Omega_{\Lambda_0} = 1. \quad (33)$$

By fitting expression 32 to the blue curve in figure 16, we obtain an indication of what kind of energy content is necessary for an approximate DI-like behaviour. We perform this fit on a single randomly generated DI model with 600 masses exhibiting generic dynamics in the LRS length evolution.

The quantities with a 0-subscript in equation (32) indicate “present day” values, obtained through observation/measurement carried out at the “present time” t_0 . We define t_0 to be the time when an observer residing in the DI universe carries out measurements or observations, indicated by the vertical dashed line in figure 16. The observer’s time is considered to progress from right to left in the figure. Consequentially, the *observer’s future* is the initially time-symmetric hypersurface at $t = 0$ and the *observer’s past* is located at large t . The notions of future and past are, with respect to the time axis in the figure, flipped in order to represent an expanding universe. Only parts of the curve where $t > t_0$ (regions to the right of the dashed line) will be fitted against using equation (32), since the observer possesses only information about the past.

By allowing the present time t_0 to progressively increase, i.e. the observer will be moved further away (temporally) from the initial time-symmetric hypersurface (located at $t = 0$), there will be less and less portions of the simulated data available for our fit. This will alter the density parameters obtained as a function of t_0 . During the fitting, Ω_M is allowed to vary freely but is restricted to non-negative real numbers.

Figure 17 depicts the density parameters Ω_{M_0} and Ω_{Λ_0} as a function of t_0 . For small t_0 , i.e. close to the initial hypersurface, we have $\Omega_{M_0} \gg 1$ which therefore results in negative Ω_{Λ_0} . The inset is an enlargement on a region where both parameters are positive simultaneously. Within this region we can have that $\Omega_{M_0} = 0.3$ (indicated by dashed red line), which corresponds well with current observations (see for instance [16]).

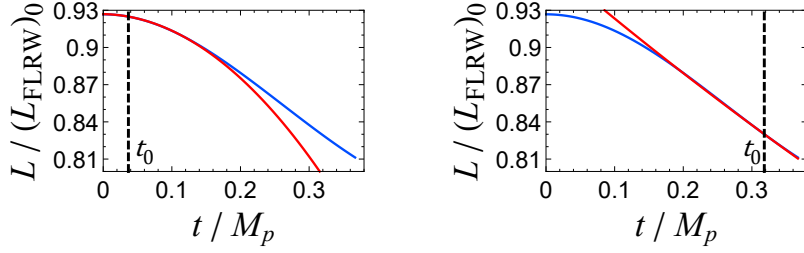


Figure 16: Examples of fitting equation (32) (red) to the LRS length in a randomly generated DI model (blue). The “present time” t_0 is progressively increased, as is visible by a shift of the vertical dashed line from left to right. The blue and red curves are tangent to each other at t_0 since we require the fitted curve to have the same H_0 and a_0 as our simulation.

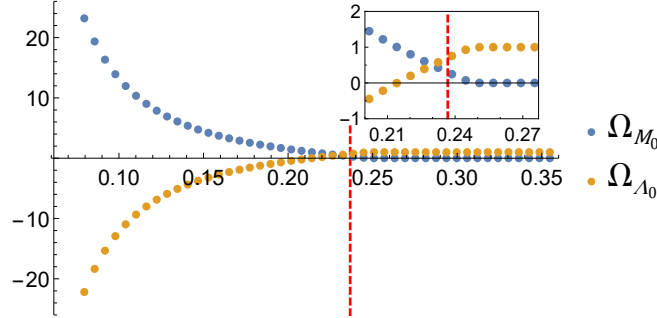


Figure 17: The relationship between the fitted density parameter Ω_{M_0} as a function of time t_0 . The value of Ω_{Λ_0} is derived using (32). At the red dashed line we obtain values $\Omega_{M_0} = 0.3$ and $\Omega_{\Lambda_0} = 0.7$.

6 Calculating the curl H -term

In this section we will estimate the curl H term and see how it evolves with time in order to determine the magnitude of the resulting error. The curl H -term in equation (22) can be evaluated recursively in a truncated Taylor series over time. The first and second order terms are zero, permitting us to stick with the third order term only, given by [9]

$$C_+^{(3)} = -n^a n^b [\text{curl curl } (E^2)_{ab}]_{t=0} t^3 \quad (34)$$

where the tensor $(E^2)_{ab}$ is defined as

$$(E^2)_{ab} = E_a^{c} E_{cb}. \quad (35)$$

Figure 18 shows an example of how the magnitude of the ODE expression (see equation (22)) compares to the curl H -term (34) as a function of time for 24 masses on a random point on the LRS curve. A general feature depicted in figure 18 is the initially zero curl H term, which makes the differential equation (22) valid for small t .

We can make some statistics of when the ODE and curl H -term are equal in magnitude. The result is shown in figure 19, where we see the median time expressed in terms of the median proper mass m_p . We managed to calculate expression (34) for configurations consisting of 8, 16 and 24 masses only. For 120 and 600 masses, the evaluating $[\text{curl curl } (E^2)_{ab}]_{t=0}$ becomes a heavy computational endeavor and is therefore omitted. However a clear pattern can be distinguished: as we increase the number of black holes, the time it takes for the ODE and curl H term to become equal increases. If we compare figure 19 with figure 10, we notice that for 600 sources it appears as if coordinate singularities appear before the curl H term becomes dominant.

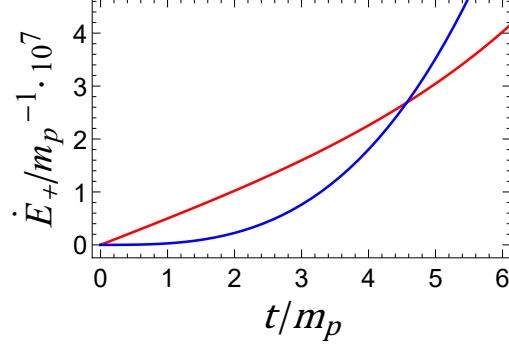


Figure 18: The red curve depicts the ODE (22), while the blue curve corresponds to the $\text{curl}H$ term (34). Notice that the $\text{curl}H$ term is very small for early t . Quantities are given in terms of the median proper mass m_p .

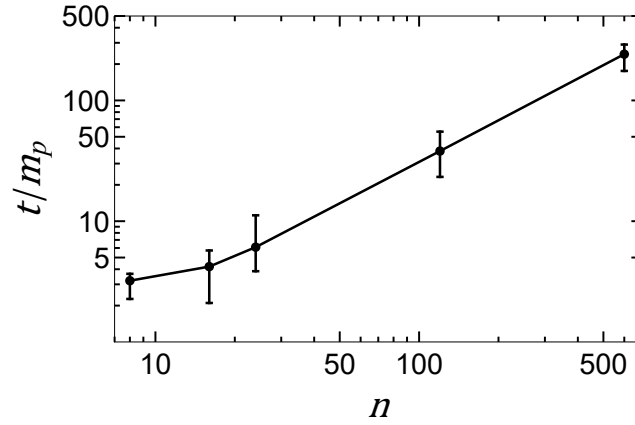


Figure 19: Plot depicting the median time it takes for the $\text{curl}H$ term (34) and ODE expression (22) to become equally large as a function of the number of sources n . The error bars indicate the quintiles.

7 Evolution with Clusters of Black Holes

7.1 Generating Clusters

In our universe, galaxies are not uniformly distributed but form instead wide networks of filaments, clusters and voids. To simulate this behaviour to some extent, we have distributed black holes on the 3-sphere in such a way to encourage the formation of clusters. The effect of discrete mass objects with some form of structure or clustering have already been investigated in for instance [22, 23, 24]. Our approach however is stochastic and will use an algorithm inspired by the two-point function used in galaxy surveys to quantify clustering [15]:

1. Focusing on one cell, distribute the desired number of black holes in a random uniform way as described in subsection 1.3.
2. Select one of the points randomly, \mathbf{P} . The probability of selecting any point is chosen to be equal.
3. Measure the distance between \mathbf{P} and every other point inside the same cell. The probability of finding a mass at point \mathbf{P} is given by the expression

$$\text{Prob}(\mathbf{P}) = 1 - \prod_{i=1}^{n-1} \left(1 - \left(\frac{d_i}{r_0} \right)^{-\gamma} \right), \quad (36)$$

where n is the number of masses, d_i is the distance on the 3-sphere between \mathbf{P} and another point \mathbf{P}_i , while r_0 and γ are parameters. This gives the probability of finding a mass at point \mathbf{P} due to other masses located at points \mathbf{P}_i .

4. Now perform a test. Generate a number, \mathbf{T} , randomly and uniformly from the interval $[0, 1]$. If $\mathbf{T} \leq \text{Prob}(\mathbf{P})$, the test is passed. Leave point \mathbf{P} alone and then proceed to pick another point at random - start at step 2. If $\mathbf{T} > \text{Prob}(\mathbf{P})$, the test is failed. Move point \mathbf{P} to another location. This new location is determined randomly according to Marsaglia's algorithm described in subsection 1.3.2.
5. Using the new location, repeat step 3 and perform the test in step 4. Repeat steps 3 and 4 until the test is passed.
6. Once the test is passed, restart at step 2.

This algorithm is repeated an arbitrary number of times. In our case, we will only generate clusters in configurations containing 600 sources and repeat the algorithm 6000 times. The parameters we used are $\gamma = 3.5$ and $r_0 = 0.05$. We will henceforth refer to the DI model without any artificial clustering as *uniform*.

7.2 Dynamics for Configurations with Clusters

Since clustering is only meaningful for many sources, we have exclusively generated clusters in configurations with 600 black holes. The LRS circumference dynamics are plotted in figure 20 in purple for 50 random configurations. A general tendency one can notice is that the purple curves are located further away from the homogenous limit given by the FLRW model, than the orange curves. The median initial length for the uniform case is $0.96(L_{FLRW})_0$ with a 60% confidence interval ranging from $0.92(L_{FLRW})_0$ to $0.99(L_{FLRW})_0$. This is closer to 1 than the clustered case, with a median of $0.82(L_{FLRW})_0$ and a confidence interval ranging from $0.76(L_{FLRW})_0$ to $0.87(L_{FLRW})_0$. In addition, the clustered models have in general a longer "lifespan". The median time for the uniform model is $0.19M_p$, but 74% of the clustered models encounter a singularity later than this. A simple explanation is that clustered groups of black holes are treated as an effective discrete mass source. This causes a "grainier" mass distribution and moves the model away from the homogenous limit.

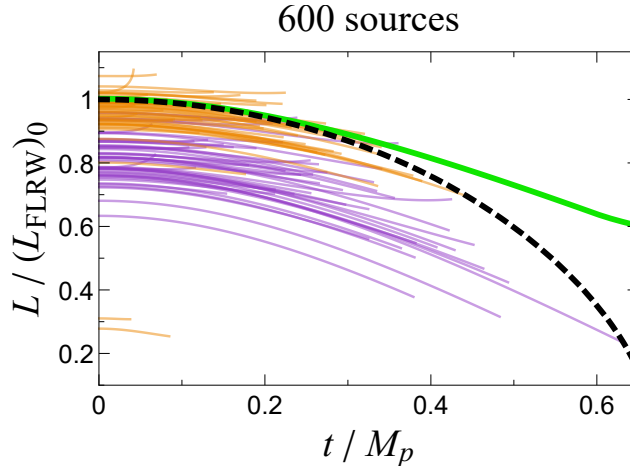


Figure 20: The LRS circumference and their evolution for four different models with 600 black holes. The purple curves correspond to the DI model with clustered configurations. The orange curves correspond to the uniform DI model with 600 sources. The black dashed curve and the green curve correspond respectively to the matter dominated spherical FLRW model and the regular model with 600 sources found in [4].

Figure 21 plots the Hubble and deceleration parameters. Turning our attention to the Hubble parameters, 60% of the clustered configurations in purple lie above the FLRW curve at $t = 0.2M_p$, compared to 98% of the uniform configurations in orange. Comparing with figure 14, decreasing the number of sources is accompanied by a decrease in the percentage of curves lying above the FLRW value at $t = 0.2M_p$, from the aforementioned 60% down to 12% for 8 sources. Thus such behaviour is more closely associated with configurations containing fewer sources than 600. This further strengthens our interpretation that a group of clustered black holes are considered as a single effective discrete mass.

8 Concluding Remarks

In earlier work on cosmological models with discrete sources, the focus has been on source distributions adapted to regular tessellations of spatial hypersurfaces. In such models, the sources reflect the regular nature of the models by being positioned at lattice centers. The LRS curves present in those models allow for a simplification of their dynamics due to the LRS symmetry. In this paper we have presented the DI cosmological model consisting of discrete sources in the form of Schwarzschild black holes having an irregular distribution. To maintain the possibility to do simplified dynamics, we have used a special tessellation of S^3 in which there is a single LRS curve. This work therefore represents a generalization of previously discussed discrete models by allowing sources to be distributed irregularly while retaining the possibility of analytic analysis of the dynamical evolution.

Our simulations suggest that initial conditions, such as the relation between total mass and size of the universe, approach the FLRW limit as the number of masses increases (see figure 4). However, the approach is slower than that of the regular models. Also, the approach in our models is from below rather than from above in the regular case. This is possibly related to the different types of tessellations used. When it comes to the dynamics, the DI models, as expected, exhibit a richer variety of behaviour than that seen in models with a regular configuration of mass sources. In fact, we find that the system is quite sensitive to the initial mass configuration. Other interesting behaviour is the appearance of negative deceleration parameters.

The DI model has proven to be a simple and flexible model which permits the investigation of a large number of discrete sources distributed in various configurations. By using DI models with a larger number of sources one could determine more precisely the relationship between initial mass configuration and the resulting dynamics. It may also be possible to improve the DI model by using

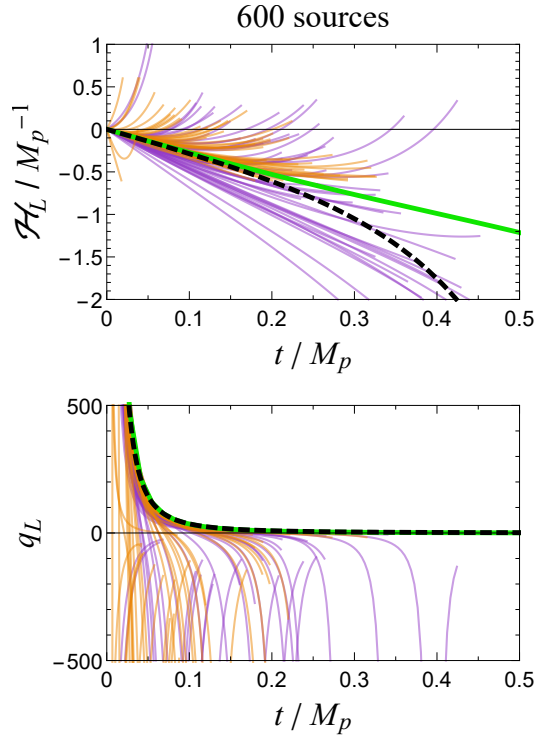


Figure 21: The above and bottom plots depict respectively the evolution of the Hubble parameter and deceleration parameter for four different models with 600 sources. The purple curves correspond to the DI model with clustered configurations while the orange curves correspond to the uniform DI model. The black dashed curve and the green curve correspond respectively to the matter dominated spherical FLRW model and the regular model with 600 sources found in [4].

geodesic slicing in order to avoid coordinate singularities. One question which is raised by the DI model is whether the expanding acceleration sometimes observed is shared by other regions beside the LRS curve. Occurrence of large scale acceleration could be due to structure formation, often referred to as cosmic backreaction, as discussed by several authors (see for example [17]). Our results for the DI models with built-in clustering show that their dynamics generally deviates more from that of the FLRW model compared to models without clustering even though the particular results for acceleration are less clear. Illuminating these issues could improve our understanding of how mass inhomogeneities affect the large scale geometry and dynamics of the universe.

One obvious drawback of our DI model is that it has a certain amount of intrinsic anisotropy. This is due to the presence of a preferred great circle as part of the construction leading to a preferred global direction. This drawback can actually be overcome by noting that besides the DI model used here it is also possible to construct DI models based on a regular lattice by the same method. To preserve the LRS property in that case when performing reflections with irregular configurations, it is necessary that the number of cells meeting at an edge is an even number. The only regular model which fulfills this requirement is the 16-cell. However, all the regular models could actually be used for this purpose if one relaxes the regularity slightly. This can be done by noting that each 3-cell in a regular tessellation is intersected by a number of symmetry planes. These planes divide the 3-cell in subcells called chambers [18]. Any two chambers in a given regular tessellation are either identical or mirror images of each other. Since adjacent chambers are related by a reflection, one can pick one chamber as the seed cell and then distribute its configuration by reflection to all the other chambers. By such a construction based on the chambers instead of the regular cells themselves, the total number of sources corresponding to a given number of sources in a seed cell can be increased significantly. For example, a regular tetrahedron has 24 chambers and so a 600-cell has $24 \times 600 = 14400$ chambers.

Acknowledgements The authors wish to thank M. Korzyński for helpful comments and a referee for constructive remarks.

References

- [1] Ellis, G.F.R., Buchert, T.: Phys. Lett. A **347**, 38-46 (2005).
- [2] Wiltshire, D.L.: Class. Quantum Gravity **28**, 164006 (2011).
- [3] Buchert, T., *et al.*: Class. Quantum Gravity **32**, 215021 (2015).
- [4] Clifton, T., Rosquist, K., Tavakol, R.: Phys. Rev. D **86**, 043506 (2012).
- [5] Bentivegna, E., Korzyński, M.: Class. Quantum Gravity **29**, 165007 (2012).
- [6] Marsaglia, G.: Ann. Math. Statist. **43**, No. 2, 645-646 (1972).
- [7] Jolin, S.W.: Dynamics of Discrete Irregular Cosmological Models, Master Thesis, Stockholm University, Stockholm (2014).
- [8] Clifton, T., Gregoris, D., Rosquist, K., Tavakol, R.: JCAP **11**, 010, (2013).
- [9] Clifton, T., Gregoris, D., Rosquist, K.: Gen. Relativ. Gravit. **49**, 30 (2017).
- [10] Ellis, G.F.R.: J. Math. Phys. **8**, 1171 (1967).
- [11] van Elst, H., Uggla C.: Class. Quantum Gravity **14**, 2673-2695 (1997).
- [12] Korzyński, M., Hinder, I., Bentivegna, E.: JCAP **08**, 025 (2015).
- [13] Bergström, L., Goobar, A.: Cosmology and Particle Astrophysics, 2nd ed., Praxis Publishing, Chichester, UK (2006).

- [14] Brill, D.R., Lindquist, R.W.: Phys. Rev. **131**, 471 (1963).
- [15] Postman, M.: Distribution of Galaxies, Clusters, and Superclusters. In: Murdin, P. (ed.) Encyclopedia of Astronomy & Astrophysics, Nature Publishing Group and Institute of Physics Publishing, London and New York (2001). <https://doi.org/10.1888/0333750888/1637>
- [16] Ade, P.A.R. *et al.*: arXiv: 1502.01589 (2015).
- [17] Buchert, T., Räsänen, S.: Annu. Rev. Nucl. Part. Sci. **62**, 57 (2012).
- [18] Borovik, A.V., Borovik, A.: Mirrors and Reflections, Springer, New York (2010).
- [19] Engström, H.: Properties of Mass Distributions for Discrete Cosmology, Master Thesis, Stockholm University, Stockholm (2013).
- [20] Gausmann, E., *et al.*: Class. Quantum Gravity **18**, 5155-5186 (2001).
- [21] Bentivegna, E., *et al.*: Class. Quantum Gravity **35**, 175004 (2018).
- [22] Korzyński, M.: Class. Quantum Gravity **32**, 215013 (2015).
- [23] Korzyński, M.: Class. Quantum Gravity **31**, 085002 (2014).
- [24] Durk, J., Clifton, T.: JCAP **10**, 012 (2017).